Nanoscale Horizons

ROYAL SOCIETY OF CHEMISTRY

COMMUNICATION

View Article Online
View Journal | View Issue

Cite this: *Nanoscale Horiz.*, 2025, **10**, 1453

Received 29th November 2024,
Accepted 2nd May 2025

DOI: 10.1039/d4nh00618f

rsc.li/nanoscale-horizons

Nucleation and arrangement of Abrikosov vortices in hybrid superconductor–ferromagnet nanostructures†

Sara Memarzadeh, * Mateusz Gołębiewski, Maciej Krawczyk and Jarosław W. Kłos

This study investigates the nucleation, dynamics, and stationary configurations of Abrikosov vortices in hybrid superconductor–ferromagnet nanostructures subjected to inhomogeneous magnetic fields generated by a ferromagnetic nanodot. Employing the simulations based on time-dependent Ginzburg–Landau coupled with Maxwell's equations, we reveal the evolution of curved vortex structures that exhibit creep-like deformation before stabilizing. The interplay between vortices and currents confined within the superconducting nanoelement gives rise to unconventional stationary vortex arrangements, which evolve gradually with increasing magnetic field strength—a behavior absent in homogeneous fields. Our numerical results illustrate how the ferromagnetic element can control vortex configurations *via* a stray magnetic field—insights that are difficult to access experimentally or analytically. We demonstrate that the superconducting nanoelement can stabilize into distinct vortex states in response to even small system perturbations. This highlights the extreme sensitivity of the system and the richness of its dynamic behaviour, revealing complex pinning mechanisms and providing valuable insights into the optimisation of nanoscale superconducting systems.

New concepts

This research introduces a novel approach to understanding vortex dynamics in hybrid superconductor–ferromagnet (SC–FM) nanostructures exposed to inhomogeneous magnetic fields. Unlike traditional studies that focus on homogeneous fields, our work reveals that the magnetic fields generated by adjacent ferromagnetic nanodots lead to complex vortex behaviors, including creeping deformation and the emergence of strongly curved stationary vortex states. By numerically solving the time-dependent Ginzburg–Landau equations coupled with Maxwell's equations, we explore how the Lorentz force, vortex interactions, and the geometric constraints of the system collectively affect the nucleation, dynamics, and configuration of vortices, behaviors not observed in the superconductor under a homogeneous magnetic field. This combination gives rise to a rich energy landscape with competing minima, leading to the stabilization of novel vortex structures. Our findings offer valuable insights into the control of vortex dynamics in hybrid SC–FM systems. This opens up new possibilities for designing superconducting devices with tailored magnetic properties. The ability to manipulate vortex configurations in nanoscale SC–FM systems is crucial for the development of advanced quantum technologies, superconducting spintronics, and magnonics, where precise control over vortex motion is essential.

1 Introduction

In type-II superconductors, an external magnetic field induces a lattice of vortices containing quantized magnetic flux, known as Abrikosov vortices, when it exceeds the critical value H_{c1}.[1,2] This effect is particularly interesting for superconductors of finite dimensions, especially those with sizes on the order of a few superconducting (SC) correlation lengths.[3–6] It has been shown that the finite size can alter the critical field, and the shape of the SC body can influence the regions of vortex nucleation. Moreover the steady-state vortex arrangement may differ from the triangular lattice observed in extended superconductors. For example, the studies in ref. 7–9 shed light on the complex interplay between magnetic and geometrical factors in SC nanostructures, particularly by comparing the vortex states in cubic and spherical geometries as a function of the magnetic field. In these cases, the vortices prefer a curved shape instead of a straight, columnar shape as seen in films. In addition, the orientation of a homogeneous magnetic field with respect to the surfaces of the SC nanoelement influences the vortex configurations,[10] as shown for the pyramidal SC nanostructures.[11]

Studies of the spatial arrangement and dynamics of vortices are essential for understanding the response of superconductors to magnetic fields[12,13] and their applications, particularly in vortex-based computing, where miniaturization is essential.[14]

Institute of Spintronics and Quantum Information, Faculty of Physics and Astronomy, Adam Mickiewicz University Poznań, Uniwersytetu Poznańskiego 2, 61-614 Poznań, Poland. E-mail: sarmem@amu.edu.pl

† Electronic supplementary information (ESI) available. See DOI: https://doi.org/10.1039/d4nh00618f

In SC systems, Abrikosov vortices can be guided or trapped in a controlled manner down to the nanoscale.[15–17] The use of vortices as information bits enables both information storage and transmission.[18] Vortex-based memory cells[19,20] are realized using nanoscopic spin valves or Josephson junctions,[21] while the introduction of artificial pinning landscapes facilitates channelized vortex transport, including unidirectional motion.[15,22–25] Nanoscopic SC fluxonic systems are already widely used as sensors, *e.g.*, magnetic microscopy, photon sensors, mainly through SC quantum interference devices (SQUIDs).[26] However, the use of Abrikosov vortices in quantum coherent circuits remains problematic due to the dissipative nature of the vortex motion, which induces decoherence.[27,28] Nevertheless, the vortices are being investigated as carriers of topological quantum information, potentially enabling the realization of Majorana states[28–30] and thus advancing quantum information processing *via* Abrikosov fluxonics.[25]

The combination of ferromagnetic (FM) and SC nanostructures, either by direct contact[31] or in separation *via* electromagnetic fields,[32] offers new possibilities to control the configurations and dynamics of both subsystems. The electromagnetic coupling includes the influence of SC currents and vortices on the magnetization configuration in the FM system,[33,34] and the effect of the stray magnetic field from the ferromagnet on the SC state.[35–42] In addition to the static effects, dynamic coupling has also been observed in superconductor–ferromagnet (SC–FM) hybrids.[43] For example, the inhomogeneous RF magnetic field of a single magnetic dipole can induce vortex semiloops in the SC nanoelement,[44] which evolve with time. Similarly, a propagating domain wall in the FM layer can push the vortices in the electromagnetically coupled SC layer,[45] while the stray field generated by the SC nanoelement or the lattice of vortices can affect the magnetization dynamics in the FM layer.[46–48]

The SC–FM hybrids with complex interactions discussed above have significant potential in spintronic[49,50] and magnonic[46,51–53] applications for non-volatile memory and logic devices. Their construction usually involves the patterned FM and SC multilayer structure, *e.g.*, in pillars as in spin valves with a hard (with fixed magnetization orientation as a spin polarizer) and a soft (with free magnetization orientation) FM layer. To be competitive with standard CMOS devices, these applications require high element densities and low currents, which necessitates element miniaturization down to the nanoscale.[49] In addition to the proximity effects at the interfaces, the influence of stray magnetic fields from the FM nanoelement on the SC state must also be taken into account.[54]

However, previous theoretical studies have mainly investigated specific factors such as the effects of a single magnetic dipole[44] and magnetic field orientations,[55] with most research focusing on systems with homogeneous magnetic fields, both in SC wires[56,57] and in nanodots.[8,9,11,58,59] As a result, the complex interplay between the nanomagnet with the inhomogeneous stray magnetic field and the nano-sized superconductor and its geometry remains an open research topic.

A key challenge in these hybrids is the complex energy landscape governing the vortex behavior, which is influenced by several factors, including: (i) the 3D geometry of the SC system, which goes beyond the simplicity of planar structures, (ii) the finite and small sizes of the SC structure, within the range of a few correlation lengths, where the external shape plays a significant role in the entire volume of the SC, (iii) the pinning mechanisms resulting from the complex energy landscape in the confined geometry while stabilizing the vortex configuration, and (iv) the inhomogeneous stray magnetic field from the finite size FM, which adds additional complexity to the SC system.

This paper fills these gaps by a comprehensive numerical study of the influence of spatially inhomogeneous magnetic fields on the vortex nucleation, their transient dynamics, and stable arrangement. Specifically, we study 3D SC nanodots exposed to the inhomogeneous magnetic fields generated by a nearby permanent nanomagnet, where both structures have the same lateral dimensions. We show that as the SC–FM hybrid structure is miniaturized to the nanoscale, the stray field from the ferromagnet develops spatial inhomogeneities in the superconductor, comparable to the size of individual vortices, which significantly affect vortex nucleation, dynamics, and steady-state configurations. To capture these effects, we solve the time-dependent Ginzburg–Landau (TDGL) equations[60–62] and Maxwell's equations using the finite element method (FEM). The time-dependent Ginzburg–Landau (TDGL) theory captures non-equilibrium phenomena by extending the static GL framework to include temporal evolution. Although difficult to observe experimentally, transient vortex dynamics reveal mechanisms behind the formation of final configurations, enriching our fundamental understanding. Interestingly, the vortex configuration that is reached in a steady state is governed by the magnetic field lines, resulting in a mixture of curved and straight vortices with the normal phase regions. The straight vortices are formed only when the average stray magnetic field magnitude exceeds a threshold value, and they are associated with the curved vortices in SC dots of larger thicknesses. These properties depend on the SC–FM separation, the lateral and vertical dimensions of the SC dot in terms of coherence length, and the penetration depth. Our research contributes to the understanding of vortex nucleation and its stable configurations in hybrid SC–FM nanostructures, which is crucial for the operation of spintronic SC devices and also devices based on the principles of Abrikosov fluxonics, where vortices are locally controlled by nanoscale ferromagnet.

The structure of the paper is as follows: in Section 2, we present the theoretical model and the computational framework used for our simulations. In Section 3, we discuss the results, first in Subsection 3.1, focusing on vortex nucleation, dynamics, and stationary configurations under inhomogeneous magnetic fields. Furthermore, we analyze the static configuration of the relaxed system as a function of the external field, in particular its magnetic properties (Section 3.2). By comparing these hybrid SC–FM systems with both SC wire and nanostructures under homogeneous magnetic fields, we

aim to elucidate the interplay between geometry and external fields, providing new perspectives on the vortex dynamics in these hybrid systems. Finally, in Section 4, we summarize the conclusions drawn from this study and suggest possible directions for future research. In addition, in the ESI,† we extend the manuscript with the details of the TDGL equation derivation, details of the numerical modeling, and numerical results for SC vortex dynamics and arrangements in different geometries.

2 Model

2.1 Method

The dynamic and static properties of the SC system are described by the TDGL equations. The TDGL theory[63,64] is formally restricted to the gapless superconductors. However, even for materials with a non-zero SC gap, the presence of impurities can broaden the singularities of the density of states and close the gap,[65] restoring the validity of the TDGL theory. Therefore, the formulation of the model based on TDGL equations is widely accepted, and effective compromise between relative simplicity and accuracy in numerical studies of SC systems and devices.[66]

While the widely used TDGL equations typically employ fully dimensionless parameters, here we use a dimensionless form for the order parameter, time and conductivity, while keeping physical units for the vector potential, external field, and spatial coordinates to preserve real-valued quantities under the magnetostatic approximation. With these transformations, the TDGL equations are:

$$\frac{\partial \psi}{\partial t} = -\frac{\lambda^2}{\kappa^2}\left(i\nabla + \frac{q}{\hbar}\mathbf{A}\right)^2\psi + \psi - |\psi|^2\psi, \tag{1}$$

$$\sigma\frac{\partial \mathbf{A}}{\partial t} = \frac{\hbar}{2iq}(\psi^*\nabla\psi - \psi\nabla\psi^*) - |\psi|^2 A - \lambda\nabla\times(\lambda\nabla\times\mathbf{A} - \mathbf{B}_\mathrm{a}). \tag{2}$$

Here, λ is the London penetration depth, ξ is the SC coherence length, $\kappa = \lambda/\xi$ is the Ginzburg–Landau parameter, $q = 2e$ is the Cooper pair charge, and $\hbar$ is the reduced Planck constant. The field of the nanomagnet is given by $\mathbf{B}_\mathrm{FM} = -\mu_0\nabla\varphi_\mathrm{M}$, with $\Delta\varphi_\mathrm{M} = \nabla\cdot\mathbf{M}$, where φ_M is the magnetostatic potential. To account for the spatial variations of the magnetic field, we replace the external field $\mathbf{B}_\mathrm{a}$ with the stray field $\mathbf{B}_\mathrm{FM}$ in the TDGL equations. This ensures a proper representation of the nanomagnet's influence on superconductivity. We solve the TDGL eqn (1) and (2) and the magnetostatic equation for FM prism using the FEM in COMSOL Multiphysics®.[67,68] Further details on the derivation of the TDGL eqn (1) and (2), the dimensionless transformations, numerical methods, time scale, and boundary conditions are provided in the ESI,† Sections S1 and S2.

We considered a uniformly magnetized, elongated nanomagnet with high saturation magnetization. The assumption of uniformity is very close to reality because of two factors: the small size (single-domain configuration) and the strong shape anisotropy (elongated FM body). It is worth noting that the stray field generated by the SC prism has a negligible effect on the static magnetization of the nanomagnet. This is because the diamagnetic response of the SC prism is strongly reduced by the finite value of London penetration depth λ. In fact, the maximum average magnetization in the SC prism (in the Meissner state) reaches only about 5% of that of the FM prism – see ESI,† Section S3, particularly Fig. S2 (ESI†). With such a small averaged field from the superconductor, the influence of the dynamic magnetic field induced in the transient state by changes in Meissner currents and moving vortices on the magnetization precession in the ferromagnet can be neglected. Moreover, in the considered system, this effect is reduced by the inhomogeneity of the static stray field of the ferromagnet, which makes the dynamics of the SC state more gradual. Therefore, we neglect the dynamical coupling in the SC–FM hybrid system in our considerations.

The vortex configuration within the SC prism, especially when exposed to the nanomagnet field, is expected to be complex, often containing poorly formed, and weakly isolated vortex structures that may merge with regions of the normal phase. Therefore, the number of vortices or even the vorticity, is no longer a reliable parameter for characterizing the SC nanoelement.[69] Instead, we quantitatively evaluate the screening properties of these SC nanostructures by their diamagnetic response, which is reflected in the volume- or surface-averaged magnetization.[7,11,58,59,70] This represents the difference between the total magnetic field $\nabla\times\mathbf{A}(\mathbf{r})$ and the applied field $\mathbf{B}_\mathrm{a}(\mathbf{r})$ within the superconductor and serves as an indicator of the demagnetizing properties:

$$\langle|\mathbf{M}|\rangle = \frac{1}{\mu_0}\frac{1}{V_\mathrm{SC}}\int_{V_\mathrm{SC}}|\nabla\times\mathbf{A}(\mathbf{r}) - \mathbf{B}_\mathrm{a}(\mathbf{r})|\mathrm{d}^3\mathbf{r}, \tag{3}$$

where $V_\mathrm{SC} = a\times a\times h$ is the volume of the SC prism. In two-dimensional simulations, the volume integrals are adjusted to the surface integrals.

To study vortex formation and arrangement, we define regions where the superconductivity, $|\psi|^2$, is significantly reduced, which will indicate vortices and indentations of normal phase. It is clear that there is no sharp boundary between these two phases, but we arbitrarily introduce a threshold value, *i.e.*, $|\psi|^2 = 0.3$, to effectively identify the boundaries between the SC and normal phases in the 3D system, as illustrated in Fig. S3 and S4 discussed in Section S3 of the ESI.† To quantify this, we introduce a filling fraction ff_N, which is the ratio of the volume in which the density of Cooper pairs $|\psi|^2$ is less than 0.3 to the volume of the SC prism:

$$ff_\mathrm{N} = \frac{1}{V_\mathrm{SC}}\int_{V_\mathrm{SC}}\Theta\left(0.3 - |\psi(\mathbf{r})|^2\right)\mathrm{d}^3\mathbf{r}. \tag{4}$$

Here, $\Theta(x)$ represents the Heaviside step function. In other words, the parameter ff_N represents the volume in which superconductivity is reduced (*i.e.* the volume of vortices and indentations of normal phase), relative to the total volume of the SC prism.

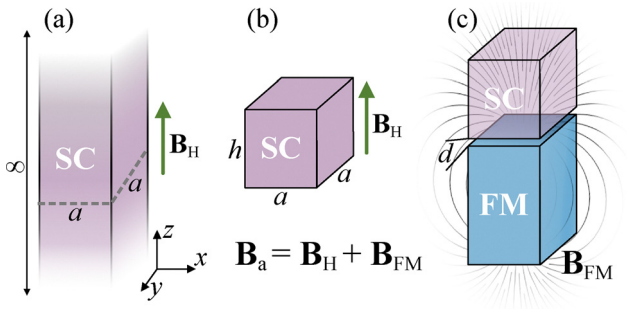

Fig. 1 Numerical studies investigate vortex configurations in a SC prism under an external magnetic field $\mathbf{B}_a$. The reference systems are: (a) an SC wire and (b) a prism of height h in a homogeneous magnetic field $\mathbf{B}_H$. (c) We focus on the effect of the inhomogeneous field $\mathbf{B}_{FM}$, generated by the FM prism, on the SC prism. The SC and FM prisms are separated by an air gap of width d, and in all studies, both the SC and FM components have the same cross-sectional area of $a \times a$.

2.2 Structure

We focus on the hybrid SC–FM structure shown in Fig. 1(c) where both the SC and FM components have a cross-sectional area of $a \times a$. The size a and the height h of the SC prism are varied, while the height of the FM prism (nanomagnet) is fixed at h_M = 700 nm. The superconductor is characterized by a GL parameter κ = 3, a penetration depth λ = 60 nm, and a dimensionless electrical conductivity, σ = 1 [expressed in the units $1/(\mu_0 D\kappa^2)$]. To get a relatively strong magnetic field from the ferromagnet, $\mathbf{B}_{FM}$, we chose its saturation magnetization to be M_s = 1350 kA m^{-1}. We tune the strength of the inhomogeneous magnetic field in the superconductor by adjusting the distance d between the it and the nanomagnet or the SC prism thickness, h. As its measure, we use the average stray magnetic field of the nanomagnet over the superconductor's volume: $\langle|\mathbf{B}_a|\rangle = \frac{1}{V_{SC}}\int_{V_{SC}} B_{FM}(\mathbf{r})\mathrm{d}^3\mathbf{r}$.

To understand the vortex nucleation and the stable configuration in the SC–FM hybrid, we consider three additional reference systems. The first one is a square cross-section SC wire under a homogeneous magnetic field B_H [Fig. 1(a)] with the dimensions $a \times a$, the same as the selected SC–FM hybrid structure. This system was simulated using a 2D model confined to the xy-plane. The infinite extension of this geometry along the z-direction ensures that the SC system does not generate a stray magnetic field outside its boundary. It not only provides a baseline for a better understanding of vortex behavior in more complex scenarios but also serves to validate the accuracy of our computational model.[57,61] The second reference system is an SC prism under a homogeneous magnetic field B_H [Fig. 1(b)], already studied in the literature,[8] with the same dimensions as the considered SC–FM system. Here, a 3D model was used to capture the already complex vortex arrangement. The final reference system is an SC sphere in an inhomogeneous magnetic field, which allows to show the differences in vortex nucleation and their stable arrangement determined by the superconductor's shape.

3 Results and discussion

The study is divided into two parts. In the first part, we investigate the process of vortex nucleation and its time evolution to a stable configuration in an SC prism placed in a nonuniform field of a nanomagnet [Fig. 1(c)].

In the second part, we focus on the studies of stable vortex configurations in different magnetic fields. For the SC prism, we tune the average applied field $B_a = \langle|\mathbf{B}_{FM}|\rangle$, in the volume of the superconductor by changing the distance to the ferromagnet, d, or the height of the SC prism, h. For the SC wire, we simply changed the magnitude of the homogeneous magnetic field, $B_a = B_H$. The results for the stable configuration are compared with the outcomes for the reference systems [Fig. 1(a) and (b)] and the SC sphere (Section S6 in the ESI†).

3.1 Vortex nucleation and transient dynamics

The dynamics of the system is studied during the transition from an initial state, in which the prism is completely in a SC state, characterized by $\psi(t = 0) = 1$ throughout its volume, to a stable configuration, in which $\frac{\mathrm{d}}{\mathrm{d}t}\psi \to 0$. At time t = 0, an external magnetic field, $\mathbf{B}_a$ (generated either by a FM nanodot, $\mathbf{B}_{FM}$, or implemented as a uniform field, $\mathbf{B}_H$), is suddenly applied, inducing a magnetic response of the SC material. The system is then allowed to evolve freely until an equilibrium is reached, where variations in the order parameter, ψ, and the vector potential, $\mathbf{A}$, are sufficiently small to be considered constant over time.

The results of such simulations are summarized in Fig. 2 (left part), which shows ff_N and $\langle|\mathbf{M}|\rangle$ as a function of time for the SC prism in the inhomogeneous field [Fig. 1(c)], drawn with red lines, and for the reference for the SC prism in the uniform field [Fig. 1(b)], drawn with blue lines. The vortex configurations (represented as regions where $|\psi|^2 < 0.3$) are shown at selected times in the right part of Fig. 2. The prism has fixed dimensions: 250 × 250 × 185 nm^3 and the mean magnetic field is 336 mT. The results for the higher prisms, *i.e.*, 250 × 250 × 205 nm^3, are shown for comparison in ESI,† Fig. S7.

Based on the $ff_N(t)$ dependence, we can see that the transition in the SC–FM structure [Fig. 1(c)], goes through four distinct stages before reaching a steady state, while in the SC prism under a homogeneous magnetic field [Fig. 1(b)], there are only three distinct stages. In the SC–FM hybrid system, the process starts from the Meissner phase throughout the whole superconductor, similar to the reference systems. The magnetic flux begins to penetrate the SC prism at the midpoints of the bottom edges, forming the indentations with a low $|\psi|^2$ (see the right part of the Fig. 2 where the regions $|\psi|^2 < 0.3$ at $t = 5\tau$ are marked), which increase with time. This process is quantified by the increase of ff_N (the upper left graph in Fig. 2). Before the transition to the mixed state, the system reaches its maximum $ff_N \cong 0.25$ at $t = 5\tau$.

In the next stage, vortices emerge from the nucleation points localized at the tops of the normal phase indentations (see ESI,† Fig. S6 at $t = 10\tau$), gradually forming curved vortices that

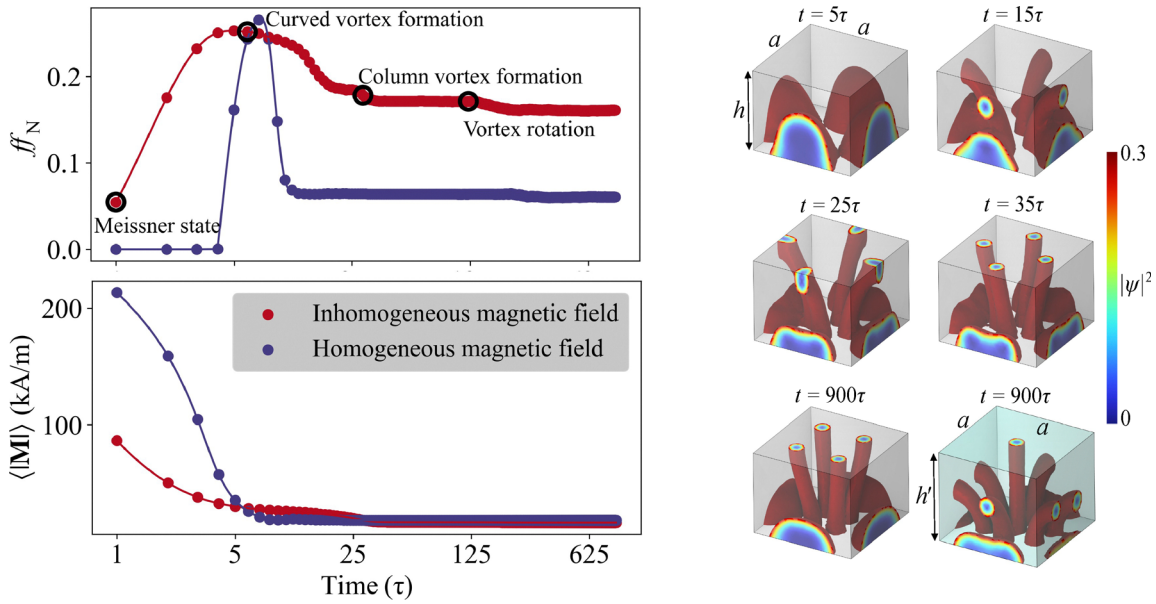

Fig. 2 Evolution of the SC prism in homogeneous and inhomogeneous magnetic fields. The upper left graph shows the time-dependent behavior of the filling fraction ff_N. The lower left graph illustrates the time evolution of the system's magnetization $\langle|\mathbf{M}|\rangle$. The right panels present the time evolution of the flux region and vortex structure in a superconductor under the inhomogeneous magnetic field of a nearby ferromagnetic nanodot. The final snapshots at $t = 900\tau$, with heights $h = 185$ nm and $h' = 205$ nm, show the vortex structures of the static system. The SC prism has a square cross-section with side length $a = 250$ nm. The SC–FM distance remains constant at $d = 10$ nm for both structures, leading to magnetic field strengths of $\langle|\mathbf{B}_{FM}|\rangle = 336$ mT for $h = 185$ nm and 315 mT for $h' = 205$ nm. For the SC prism in a homogeneous magnetic field $\mathbf{B}_H = |\mathbf{B}_{FM}|$.

elongate and change their curvature as their ends climb up the lateral faces of the SC prism (see the vortex configuration at $t = 15\tau$). Finally, all the vortices reach the top surface of the prism at $t = 25\tau$. The analysis of the $ff_N(t)$ dependence shows that this parameter decreases significantly until the end of this stage $t = 25\tau$. The dynamics in the stage, when the curved vortices are nucleated and grow towards the top face of the SC prism, *i.e.*, from $t = 5\tau$ to 25τ can be considered, in analogy to mechanical,[71] FM[72] or ferroelectric[73] systems, as a creep-like deformation[74] (see also the discussion in Section S7 of the ESI†).

These two initial stages are significantly different for the SC prism exposed to a homogeneous external magnetic field, *i.e.*, the structure shown in Fig. 1(b) (see the red curves in Fig. 2). Here, the columnar vortices nucleate quite abruptly from the sides of the prism (at $t \approx 5\tau$) and are fully formed with the lengths determined by the height of the structure. In this case, the time from the nucleation to the formation of column vortices is only about $\Delta t = 5\tau$ compared to the much longer time $\Delta t = 15\tau$ of the creep-like dynamics in the inhomogeneous case [see plot of $ff_N(t)$ in Fig. 2]. Thus, as expected, straight vortices are energetically favorable in the homogeneous magnetic field system (see also Fig. S6 in the ESI†).[75]

In the third stage of the evolution of SC–FM heterostructures towards a stable vortex configuration, the vortices migrate inwards from the edges of the top surface during the time change from $t = 25\tau$ to $t = 35\tau$ (see Fig. 2). As a result, the initially curved vortices gradually straighten out but remain curved even in the final phase (see the visualization at $t = 900\tau$). At this stage, we observe a further reduction of ff_N to $\cong 0.17$. If the prism height is increased while keeping the lateral dimensions the same, more vortices remain strongly curved and their outlets do not reach the top face of the prism in the steady state, as shown in the lower right sub-figure of Fig. 2 and also in Fig. S7 of the ESI.†

In the final stage of the evolution, just before reaching the static state, the vortex columns begin to rearrange themselves, rotating by 45 deg around the vertical axis of the prism (compare the plots of $|\psi|^2$ in Fig. 2 at $t = 35\tau$ and $t = 900\tau$). In this phase, the filling factor decreases only slightly to the value $ff_N \cong 0.16$. A similar rotation and rearrangement of the columnar vortices is also observed in the SC prism in a uniform field, as shown in Fig. S6 in ESI,† Section S4 (ESI†). However, here the ff_N remains almost unchanged and at a much lower level, *i.e.*, $ff_N \cong 0.08$. This behavior optimizes vortex penetration, minimizes repulsive vortex energy, and also creates space for vortex nucleation when the bias magnetic field is increased (see discussion in the next section).

The above described changes in ff_N during nucleation and vortex stabilization are followed by changes in the magnetization $\langle|\mathbf{M}|\rangle$, as shown in the lower left plot in Fig. 2. For the SC prism in a homogeneous magnetic field, the magnetization of the SC prism drops sharply from the high value of ~ 213 kA m^{-1} to 18 kA m^{-1} at $\Delta t = 8\tau$ after vortex formation and stabilizes before the vortices undergo rotation. In contrast, for the SC prism placed in an inhomogeneous magnetic field (SC–FM hybrid structure), the decrease in magnetization is more gradual, from ~ 86 kA m^{-1} to 18 kA m^{-1} over $\Delta t = 26\tau$. However, unlike the ff_N curve, the time evolution of the magnetization does not show clear intermediate steps.

Behind the described vortex nucleation and their formation in a columnar structure, there is a complex mechanism driven by the interplay between the applied magnetic field, SC currents, vortex interactions, and the geometry and size of the SC body.[76–78] Nevertheless, the observed differences between the SC prism in non-uniform and uniform external magnetic fields (see the direct comparison of the vortex configuration relaxation under both homogeneous and inhomogeneous external fields in ESI,† Section S4) suggest a correlation between the vortex bending and the direction of the external magnetic field lines.[2,79,80] Although we cannot provide a complete description and explanation of this effect, we propose intuitive arguments below to help understand it.

In the GL free energy functional outlined in eqn (S1) (ESI†), the term $\left|\left(\nabla - \frac{iq}{\hbar}\mathbf{A}(\mathbf{r},t)\right)\psi(\mathbf{r},t)\right|^2$ represents the kinetic energy, which captures the interaction between the spatial variation of the order parameter and the vector potential. The last term, $|\mathbf{B} - \mathbf{B}_a|^2$, quantifies the magnetic energy density and measures the energy cost associated with the deviation of the total magnetic field [$\mathbf{B}(\mathbf{r}, t) = \nabla \times \mathbf{A}(\mathbf{r}, t)$] from the external field ($\mathbf{B}_a$) and it is crucial for understanding vortex stability.

When the order parameter gradient, $\nabla\psi(\mathbf{r}, t)$, associated with the SC current circulation around the vortex core, aligns with $\mathbf{A}(\mathbf{r}, t)$, it indicates that the vortex core is oriented along the local magnetic field lines [$\nabla \times \mathbf{A}(\mathbf{r}, t)$]. This orientation minimizes the term $i\mathbf{A}(\mathbf{r}, t)\cdot\psi^*(\mathbf{r}, t)\nabla\psi(\mathbf{r}, t)$ in the kinetic energy, and $|\nabla \times \mathbf{A}(\mathbf{r}, t) - \mathbf{B}_a|^2$ in the magnetic energy, which increases the stability of the vortex. Physically, if the vortices are misaligned with the applied magnetic field lines, the interaction between the magnetic field and the supercurrent associated with the vortices leads to an increase in the magnetic energy. Consequently, the vortices have a strong tendency to align with the magnetic field lines to minimize energy.

However, as the vortex bends, the order parameter gradient $\nabla\psi$ undergoes rapid spatial variations, leading to an increase in $|\nabla\psi|^2$ and hence higher kinetic energy. Furthermore, in the context of the TDGL equation, the term $\nabla^2\psi$ can be interpreted as a curvature contribution to the kinetic energy, further increasing the energy associated with the vortices. It is important to recognize that the curvature of the vortices distorts the supercurrent distribution [as expressed in eqn (S5), ESI†], which is fundamentally related to $\nabla\psi$. Therefore, the presence of curved structures imposes an increase in energy, while straight configurations are energetically favored due to their ability to maintain a more uniform supercurrent distribution.

In light of this, we identified two opposing effects, one favoring the alignment of vortex lines along the biased magnetic field lines and the other favoring straight columnar vortices. While vortices attempt to align with magnetic flux lines, columnar flux line configurations serve as the preferred structure, illustrating the tendency of vortices to migrate toward straighter flux lines during the third phase of the vortex transition process (Fig. 2 at $t = 35\tau$). Nevertheless, we must keep in mind that in an SC system characterized by nanoscale size and subjected to an inhomogeneous magnetic field, the vortex configuration is additionally imposed by other effects, *e.g.* (i) the inhomogeneity of the Lorentz force acting on the vortices, resulting from variations in the Meissner current density circulating in the SC material, and (ii) the vortex–vortex interactions, which depend in confined geometry on the absolute position of the vortices. Consequently, the stationary state of the vortex configuration is determined by the balance between the different effects, which includes both the deformation of individual vortices and their interactions.[2,79,80]

3.2 Magnetization in the stationary state

In this subsection, we demonstrate how the steady state of the hybrid SC–FM system evolves as we increase the strength of the external field. The initial conditions for each simulation are set to $\psi(t = 0) = 1$, with either $\mathbf{B}_a(t = 0) = \mathbf{B}_{FM}$ or $\mathbf{B}_H$, assuming the abrupt application of the magnetic field. For comparison, we also simulate the SC prism and the infinite SC wire, both in a homogeneous magnetic field along the *z*-axis.

We refer first to the results for the SC square wire [Fig. 1(a)] under a homogeneous magnetic field shown in Fig. 3(a). In the Meissner state, *i.e.*, for fields smaller than the first critical field B_{c1}, where no stable vortex is present, the filling fraction ff_N remains close to zero, and the magnetization is proportional to $\mathbf{B}_H$ due to the increasing Meissner current density at the wire surfaces [see the insets in Fig. 3(a) at B_H = 100 mT and 255 mT]. For fields greater than B_{c1}, each mid-side acts as an equivalent nucleation center, allowing the simultaneous nucleation of vortices in groups of four, as indicated by the numbers 4, 8, and 12 in Fig. 3(a). Changing the number of vortices significantly alters the magnetization of the system and the values of the ff_N. The fields corresponding to the step decrease in magnetization (due to the formation of the new vortices and the shielded supercurrent) and the step increase in filling fraction (to ff_N = 0.25, 0.36, and 0.55) coincide with the minimum field values at which the system supports 4, 8, and 12 vortices in the steady state, *i.e.*, B_H = 260, 415, and 550 mT, respectively. As the field increases between the formation of additional vortices, the Meissner currents gradually increase again until the Lorentz forces acting on the vortices are strong enough to induce their 45 deg rotation around the vertical axis (compare the insets at B_H = 260 mT and 407 mT).

The symmetric process of vortex entry in groups of four can be disturbed by many factors. For example, if the magnetic field changes semi-adiabatically, *i.e.*, with $\psi(t = 0)$, each step is taken from the steady state of the previous step at a slightly lower field. In this case, for the field step ΔB_H = 5 mT, only the first vortices nucleate in a group of four as shown in ESI,† Fig. S8. Here, the number of simultaneously nucleated vortices depends on the symmetry of the previous vortex configuration and the interactions between the vortices. Another example is the SC wire with a defect, *e.g.*, a notch in the middle of one side of the wire. It breaks the fourfold symmetry and allows individual nucleation and stabilization of vortices with increased magnetic field (see, ESI,† Fig. S8). In the following paragraphs, we will see a similar effect in the SC prism placed in homogeneous and especially inhomogeneous magnetic fields.

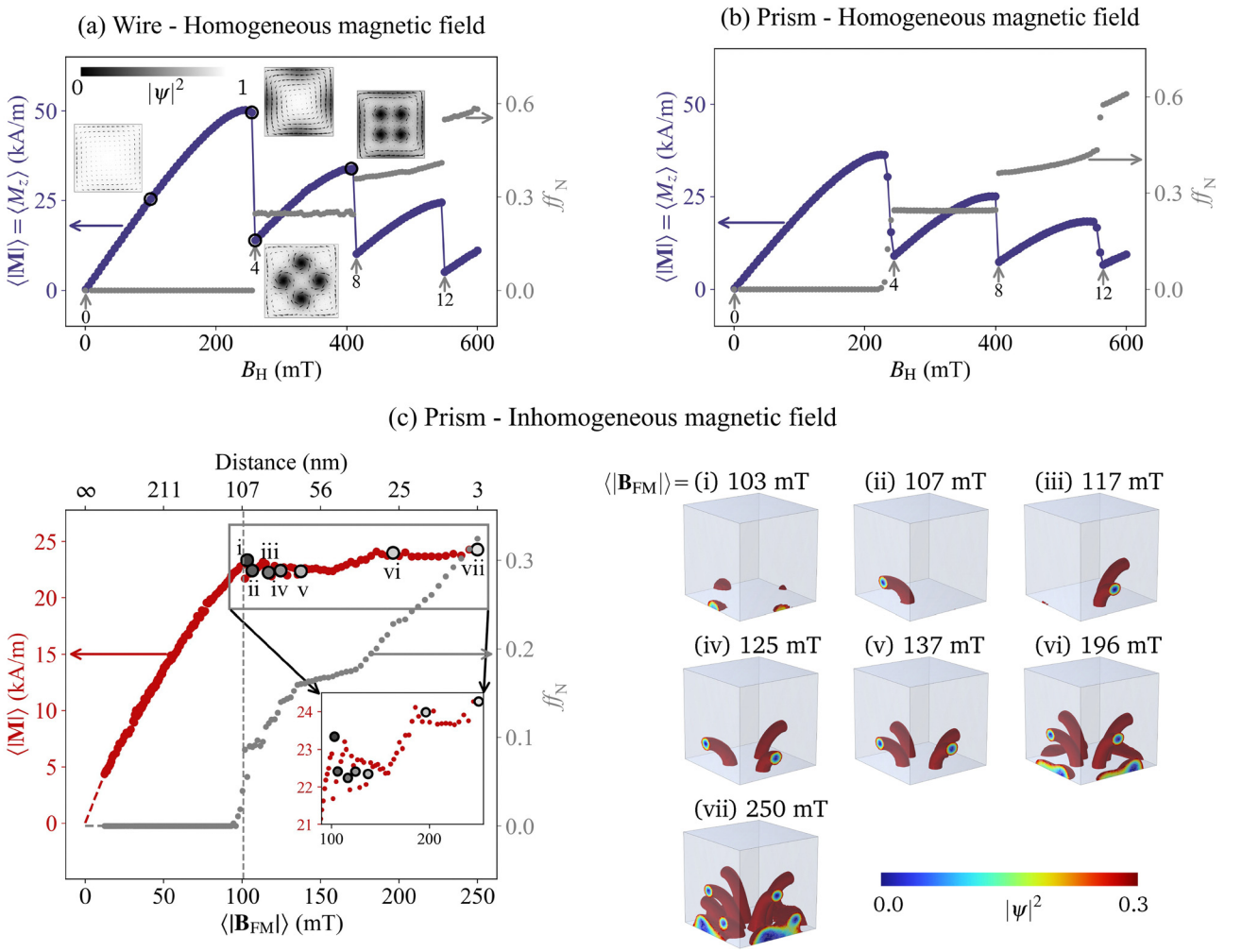

Fig. 3 Dependence of average magnetization, filling fraction, and vortex structure in superconductors with different geometries on magnetic field: (a) average magnetization $\langle|\mathbf{M}|\rangle$ (blue) and vortex density ff_N (gray) *vs.* homogeneous magnetic field $B_a = B_H$ for the wire. Transitions are marked by gray arrows, highlighting where the number of vortices changes. Insets show vortex patterns and supercurrent distribution as cones at different fields. (b) As in (a), but for the SC prism in homogeneous fields, $B_a = B_H$. (c) SC prism under an inhomogeneous field from a nearby FM. The graph depicts $\langle|\mathbf{M}|\rangle$ (red) and ff_N (gray) *vs.* the average magnetic field $\langle|\mathbf{B}_{FM}|\rangle$ (bottom axis), or equivalently *vs.* separation between the superconductor and the ferromagnet (top axis). The gray dashed line represents the point where the first vortex appears. Visualizations (i)–(vii) show static vortex configurations with vortex adaptation as distance decreases. In all cases, the SC structure has a square prism shape with a base of 250 × 250 nm^2 and a height of 320 nm. The values $\langle\cdots\rangle$ are averages over the superconductor's volume (3D) or surface (2D).

Indeed, in the SC prism in a homogeneous field [Fig. 3(b)], we observe metastable configurations with 1, 2, 3, or 5 vortices appearing in narrow field ranges.[8] Notably, the magnetization of the infinite wire (maximum at 50 kA m^{-1}) generally exceeds that of the prism (maximum at 36 kA m^{-1}), indicating larger average Meissner currents. This difference can be attributed to the absence of stray fields outside the boundary in the SC wire, which enhances the Meissner effect and preserves the fourfold symmetry.

In the hybrid SC–FM system [Fig. 3(c)], a non-uniform magnetic field introduces significant complexity in the stationary vortex configuration compared to the uniform field scenario [Fig. 3(b)]. This change is already evident in the rather continuous dependence of $\langle|\mathbf{M}|\rangle$ and ff_N on the applied field strength shown in Fig. 3(c). For the considered structures, B_{c1} is 260 mT for the SC wire (a), 235 mT for the SC prism (b), and 100 mT for the SC–FM (c), as indicated by the left vertical dashed line in Fig. 3(c). Similarly, the maximum value of $\langle|\mathbf{M}|\rangle$ is 50 kA m^{-1} for structure (a), 36 kA m^{-1} for structure (b), and 24 kA m^{-1} for structure (c). It is evident that the magnetization values for the hybrid system decrease compared to the homogeneous field scenarios. Even the infinite wire, which theoretically provides optimal magnetic shielding, shows a response that is significantly weaker than perfect diamagnetism. This limitation is attributed to the finite London penetration depth and the small dimensions of the superconducting material, as discussed in ESI,† Section S3.

Let us discuss in more detail the evolution of the vortex arrangement as a function of the field of the hybrid system shown in Fig. 3(c). For the field $\langle|\mathbf{B}_{FM}|\rangle \approx 100$ mT, we observe a

stationary configuration with four normal phase indentations located at the centers of the lower edges, where the density of Meissner currents is highest [see label (i)]. As we relax the system at slightly higher fields, we observe the emergence of one (ii) at $\langle|\mathbf{B}_{FM}|\rangle$ = 107 mT, two (iii) at $\langle|\mathbf{B}_{FM}|\rangle$ = 117 mT, three (iv) at $\langle|\mathbf{B}_{FM}|\rangle$ = 125 mT, and finally four (v) $\langle|\mathbf{B}_{FM}|\rangle$ = 138 mT curved mini-vortices, effectively expelling the remaining normal phase indentations. The selection of faces for mini-vortex formation in configurations (ii), (iii), and (iv) is random, influenced by symmetry breaking due to numerical approximations, such as mesh asymmetry and numerical procession. In a real sample, it may be due to any structural imperfections. As more curved vortices develop, the overall screening of the SC prism decreases, resulting in a downward trend in the $\langle|\mathbf{M}|\rangle$. As the applied field increases beyond the levels seen in configuration (v), the screening can exceed that in configurations (ii)–(v), resulting in an enhanced diamagnetic response in the system. This enhancement is reflected in the increased magnetization $\langle|\mathbf{M}|\rangle$ [see inset in Fig. 3(c)]. At even higher fields, the normal phase begins to penetrate the SC prism at its bottom edges (vi), further complicating the overall screening effect.

It is important to note that the maximum field value $\langle|\mathbf{B}_{FM}|\rangle \approx 250$ mT [bottom axis in Fig. 3(c)] corresponds to a small separation of 3 nm between the nanomagnet and the SC prism (top axis). To further increase the $\langle|\mathbf{B}_{FM}|\rangle$ would require unrealistically high saturation magnetization values for the nanomagnet, given the current system geometry. However, in such fields, we expect to see an expansion of the normal phase indentations and/or an increase in vorticity, a deterioration of the screening, and ultimately a loss of superconductivity throughout the SC sample, which could manifest itself in a decrease in magnetization, as observed in the SC wire and SC prism.

The changes related to the emerging new vortices are also observed in $ff_N(\langle|\mathbf{B}_{FM}|\rangle)$ dependence. Starting from configuration (i), as the system transitions to the mixed state, the filling fraction gradually increases from zero in the Meissner state. This increase signifies the penetration of the magnetic field, leading to a gradual change in the SC state rather than a sudden vortex formation. These results indicate that the energy landscape in the SC–FM system is highly complex.

We also consider how general the properties discussed in Fig. 3 are. Fig. 4 shows results for a hybrid SC–FM system with an enlarged cross-sectional area of 350 × 350 nm^2 for both the SC prism and the nanomagnet, keeping the superconductor's height, SC–FM distance, and material parameters the same. With the increased lateral dimensions of the system, there is a greater capacity for a higher number of vortices, including those that are less curved. The increased cross-section of the nanomagnet produces a more uniform magnetic field at the center of the SC prism cross-section. This supports the columnar vortices, as discussed above. Accordingly, it results in a gradual increase of the filling fraction with increasing the external field (shown as the gray curve in Fig. 4), which reinforces the previous observations of continuous changes. Considering $\langle|\mathbf{M}|\rangle(\mathbf{B}_a)$, similar behavior to the smaller SC prism is observed, including a decrease in magnetization at about 100 mT, which is higher than B_{c1}. However, in the current system, the presence of columnar vortices induces a slight reduction in the magnetization ($\approx$ 2 kA m^{-1}). The stationary vortex configurations containing the same number of columnar vortices, exhibit comparable magnetization as can be seen in the configurations represented by the same color in Fig. 4(c) [each data point in the $\langle|\mathbf{M}|\rangle(\mathbf{B}_a)$ plot is color-coded according to the number of columnar vortices in the corresponding vortex configuration]. Overall, as the magnetic field increases above B_{c1}, there is a clear downward trend in $\langle|\mathbf{M}|\rangle$, consistent with the behavior shown in Fig. 3(a) and (b).

From an experimental point of view, it may be more convenient to control the average magnetic field by the thickness of the SC prism rather than by the SC–FM separation. The influence of the SC prism thickness h on vortex formation and magnetization (keeping a = 350 nm and d = 100 nm fixed) is shown in Fig. 4(c) and (d). With decreasing h (or increasing $\langle|\mathbf{B}_{FM}|\rangle$), the magnetization shows discrete drops, which are associated with the generation of additional columnar vortices (their number is encoded in the color). Interestingly, the magnetization drop between configurations becomes larger as the superconductor's height decreases. The rapid decrease of $\langle|\mathbf{M}|\rangle$ observed for $h < 60$ nm is additionally related to the reduction of Meissner screening near the superconductor surface at distances comparable to the London penetration depth λ = 60 nm.

Fig. 4(d) illustrates selected vortex configurations for different superconductor's thicknesses. As the height of the SC prism h decreases from 340 nm to 30 nm, there is a distinct transition from a fully 3D vortex configuration to a quasi-2D vortex arrangement, similar to the Abrikosov lattice in thin SC films under uniform magnetic fields. This transition occurs for $h \approx$ 123 nm ($\langle|\mathbf{B}_{FM}|\rangle \approx 250$ mT). The evolution of the vortex state is a result of the decreasing inhomogeneity of the magnetic field, along the height of the SC prism, and the increasing value of the average magnetic field $\langle|\mathbf{B}_{FM}|\rangle$, inside the prism, which affect the curvature and the number of vortices, respectively. Comparing the $\langle|\mathbf{B}_{FM}|\rangle$ average magnetization dependencies in Fig. 4(a) and (c), we can see that while the general trend is the same in both dependencies, there are important differences in the vortex configurations for the same average magnetic fields but different SC–FM separations and superconductor's thicknesses [compare respective plots in Fig. 4(b) and (d)]. This clearly confirms that in addition to the average parameters describing the magnetic field, its inhomogeneity in the volume of the superconductor is an important factor influencing the SC state.

There is another interesting property of the complex energy landscape observed in nanoscale hybrid SC–FM systems. It is a multiple local minima at similar magnetic fields but corresponding to different vortex configurations. It is indicated by different groups of the vortex arrangements overlapping the same range of $\langle|\mathbf{B}_{FM}|\rangle$ as shown in the insets in Fig. 3 and 4 (sets of identically colored points). In examining this observation, we note that for a given applied field, the system can relax

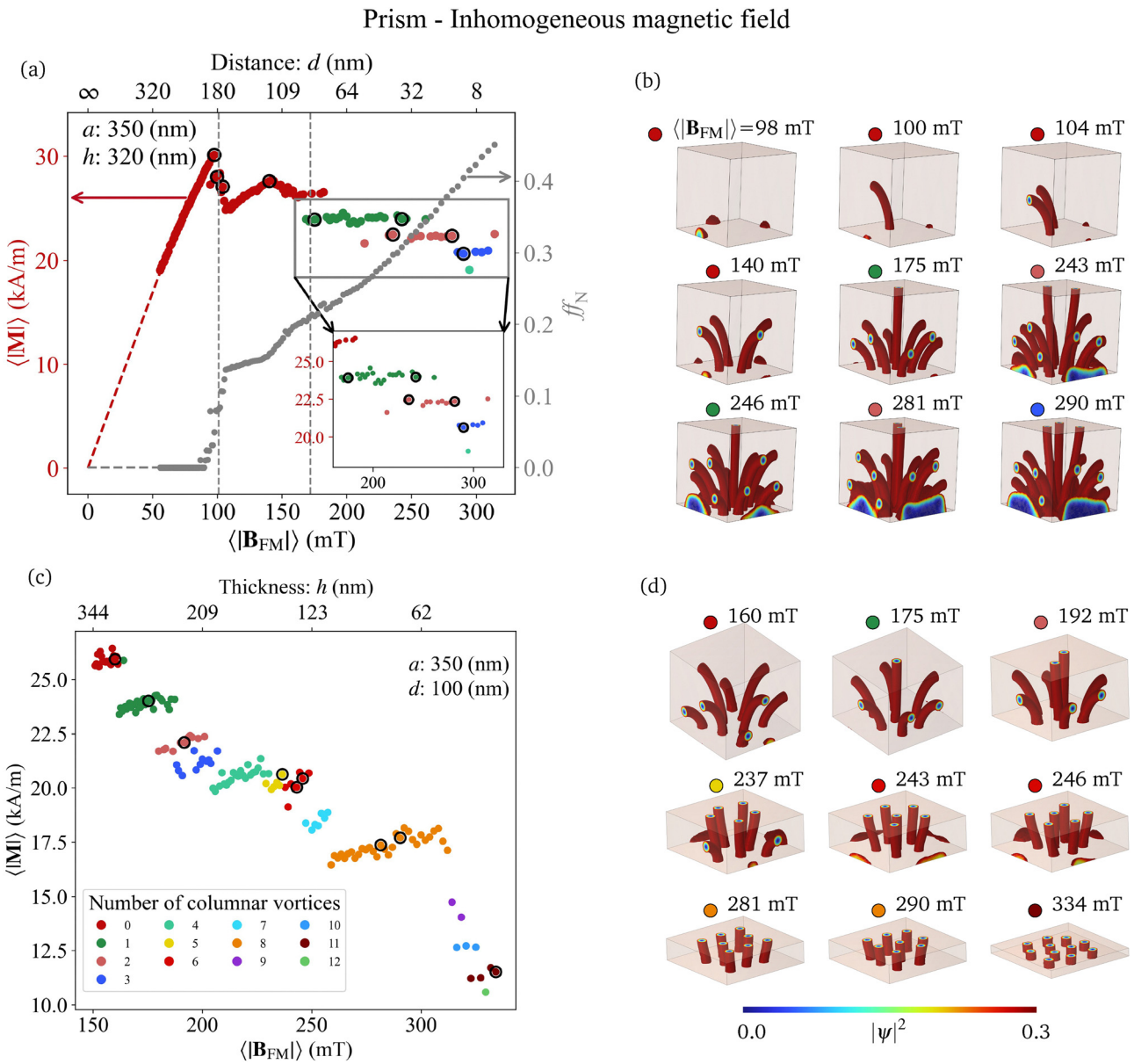

Fig. 4 (a) The graph shows the average magnetization $\langle|\mathbf{M}|\rangle$ (color corresponds to the number of columnar vortices) and the filling factor ff_N (gray) plotted against the average magnetic field $\langle|\mathbf{B}_{FM}|\rangle$ (SC–FM separation, d) for a SC prism. The first gray dashed line represents the first critical field, and the second gray dashed line indicates where the first curved vortex becomes straight. (b) Visualizations of the static vortex configurations at selected field values. The SC structure has a square prism shape with a base of 350 × 350 nm^2, with a fixed SC height, h = 320 nm. (c) The graph shows the average magnetization $\langle|\mathbf{M}|\rangle$ as a function of the average magnetic field $\langle|\mathbf{B}_{FM}|\rangle$, for different superconductor thicknesses, h, with a fixed base size of 350 × 350 nm^2 and a constant SC–FM vertical separation of d = 100 nm. Each color represents a different number of stabilized columnar vortices in the final vortex state. (d) Visualizations of the three-dimensional vortex configurations corresponding to selected values of the averaged applied magnetic field for different heights of the SC prism. The configurations were plotted for selected heights h and corresponding values of averaged magnetic fields $\langle|\mathbf{B}_{FM}|\rangle$, marked by open dots in (c).

into several configurations defined by different numbers of columnar vortices. For instance, in Fig. 4(b) the configurations for B_{FM} = 243 mT and 246 mT are influenced by nearby magnetic fields, suggesting that the system, starting from an initial state of ψ = 1, can follow several equivalent paths to minimize its energy, eventually reaching different energy minima.

Furthermore, we investigated the stabilization of vortices in the SC sphere of similar volume as in Fig. 4 in an inhomogeneous magnetic field – see details in the ESI,† Section S6. We found that, depending on $\langle|\mathbf{M}|\rangle(\langle|\mathbf{B}_{FM}|\rangle)$, there is a fairly clear sequence of overlapping magnetization levels after passing the first critical field, related to the configurations that differ in the number of vortices (similar to the prisms, discussed above). Overlapping means that, as in the case of the SC–FM prism, we can stabilize a different number of vortices by relaxing the system in a given field. This allows us to assume

that the existence of multiple local energy minima in the same inhomogeneous field, corresponding to different vortex configurations, is a general property.

The realistic scope of this investigation must take into account for factors such as temperature effects, vacancies, impurities, and interface roughness, all of which affect vortex dynamics and static configurations. The role of pinning centers, resulting from imperfections, is often considered and can have varying effects depending on the strength of the pinning relative to the thermal energy of the system. If it exceeds the pinning strength, no significant changes in the vortex configuration are expected, although the time to reach equilibrium will be longer. If the pinning strength is much greater than the thermal energy, vortices may be trapped at these centers. However, each influencing factor requires extensive research, which is beyond the scope of this study.

4 Conclusions

By solving the TDGL equations, we have numerically studied the nucleation and arrangement of SC vortices in the hybrid structure composed of an SC prism magnetically coupled with a FM prism of the same square cross section. The system studied was small in size, on the order of a few correlation lengths. We found that vortex nucleation in the non-uniform field of the FM prism begins with small curved vortices at the lower edges of the SC prism, just above the ferromagnet. The vortices then gradually increase in length toward the top face of the SC prism by creeping along its sides. This creep-like deformation results from the impact of the stray magnetic field on the SC prism and from vortex–vortex interactions. Eventually, some of the vortices reach the upper surface and form columnar vortices located in the central part of the prism's vertical cross-section. We observed that the vortices follow the lines of the external magnetic field and provided an intuitive explanation for this effect. We think that the numerical studies on the transient dynamics in 3D SC nanostructures provide insight into the process of vortex stabilization, giving clues as to how this configuration is achieved and how it can be controlled by external fields. This knowledge is important for both the fundamental understanding and the practical applications of 3D fluxonics, and remains difficult to obtain through theoretical or experimental studies.

We noticed that the SC prism, when relaxed in a non-uniform external field of a given strength, can reach one of a few stationary states that differ in the number of columnar vortices. Such ambiguity in the selection of the stationary state is not observed for the SC prism exposed to a uniform field. We think that for the SC nanodots placed in a non-uniform field, the geometric pinning of the vortices is stronger and the vortex configuration can be more easily locked into one of the few competing energy minima than in the case of the SC system placed in a uniform field. Furthermore, we found that the presence of columnar vortices is essential for the degradation of the demagnetizing properties of the SC prism. This is manifested by a rather strong reduction of the average magnetization. Our results show that the same system, tested numerically under nearly identical conditions, can stabilize in one of several vortex configurations that differ significantly in average magnetization. This demonstrates its sensitivity to minimal changes that may arise in experimental systems from weak defects, small surface/interface imperfections, or even from thermal fluctuations.

Our work is particularly relevant in the context of the recent experimental realization of the SC nanostructures,[55] which demonstrated that the curvature of vortices is strongly influenced by both the orientation and strength of the applied magnetic field, with higher magnetic fields tending to straighten the vortices. Experimental studies of the SC vortex arrangements can be performed using various types of scanning microscopes, including STM,[81,82] MFM,[83,84] SQUID,[16,85] and scanning Hall probe microscopy.[23] However, it remains a challenge to find an experimental technique capable of capturing the fast dynamics of individual vortices.[85] Nevertheless, our numerical simulations provide insight into the complex transient dynamics of vortex configurations, helping to elucidate the mechanisms behind their nucleation and stabilization. Although the 3D visualization of curved vortices is challenging nowadays, a promising way can be the use of magnetic tomography based on XMCD, which can achieve a spatial resolution of 15 nm[86] and operate at low temperatures.[87]

We hope that future experimental research will validate our findings and explore improved control over vortex dynamics. This is important for the development of various types of fluxonic devices. Considering this field, our research can be extended to asymmetric nanostructures, including those in which a superconductor is placed in an inhomogeneous and asymmetric field of a nanomagnet. Such a SC nanoelement with asymmetric pinning could serve as a diode for vortices, when connected to SC electrodes. The rectification effect[22] should be enhanced in this case, considering that a 3D structure with bent vortices can increase the pinning asymmetry.

Author contributions

J. W. K. conceived the initial idea for the project and supervised the research. S. M. developed the core concepts for the simulations, performed the computations, and drafted the manuscript. M. K. provided additional supervision and guidance throughout the project. M. G. assisted in verifying the simulations and designed the figures. All authors discussed the results and contributed to the final version of the manuscript.

Data availability

Data supporting this study are openly available from the repository: **https://doi.org/10.5281/zenodo.14045919**.

Conflicts of interest

There are no conflicts to declare.

Acknowledgements

The authors would like to thank A. Gulian and O. Dobrovolskiy for fruitful discussions. We also thank P. Graczyk for his valuable assistance with the numerical simulations. The work was supported by the grants of the National Science Center – Poland, No. UMO-2021/43/I/ST3/00550 (S. M. and J. W. K.) and UMO-2020/39/I/ST3/02413 (M. G. and M. K.).

Notes and references

1 A. A. Abrikosov, *Phys. Chem. Solids*, 1957, **2**, 199–208.
2 E. H. Brandt, *Rep. Prog. Phys.*, 1995, **58**, 1465.
3 A. K. Geim, I. V. Grigorieva, S. V. Dubonos, J. G. S. Lok, J. C. Maan, A. E. Filippov and F. M. Peeters, *Nature*, 1997, **390**, 259–262.
4 L. F. Chibotaru, A. Ceulemans, M. Morelle, G. Teniers, C. Carballeira and V. V. Moshchalkov, *J. Math. Phys.*, 2005, **46**, 095108.
5 B. Xu, M. V. Milošević and F. M. Peeters, *Phys. Rev. B: Condens. Matter Mater. Phys.*, 2008, **77**, 144509.
6 H. Baek, J. Ha, D. Zhang, B. Natarajan, J. P. Winterstein, R. Sharma, R. Hu, K. Wang, S. Ziemak, J. Paglione, Y. Kuk, N. B. Zhitenev and J. A. Stroscio, *Phys. Rev. B: Condens. Matter Mater. Phys.*, 2015, **92**, 094510.
7 G. R. Berdiyorov, A. D. Hernandez and F. M. Peeters, *Phys. Rev. Lett.*, 2009, **103**, 267002.
8 L. Peng, C. Cai and C. Chen, *J. Supercond. Novel Magn.*, 2017, **30**, 2059–2064.
9 L. Peng, C. Cai, J. Lin, J. Chen, Y. Liu and Y. Zhou, *J. Supercond. Novel Magn.*, 2016, **29**, 1197–1201.
10 E. H. Brandt, *Phys. Rev. B: Condens. Matter Mater. Phys.*, 1993, **48**, 6699–6702.
11 A. Hasnat, *J. Supercond. Novel Magn.*, 2020, **33**, 575–582.
12 M. Tinkham, *Introduction to superconductivity*, McGraw-Hill, Inc., New York, 1996.
13 N. Kopnin, *Theory of nonequilibrium superconductivity*, Clarendon Press, 2001.
14 J. M. D. Teresa, *Mater. Quantum Technol.*, 2023, **3**, 013001.
15 R. Wördenweber, *Phys. Sci. Rev.*, 2017, **2**, 20178000.
16 I. Keren, A. Gutfreund, A. Noah, N. Fridman, A. Di Bernardo, H. Steinberg and Y. Anahory, *Nano Lett.*, 2023, **23**, 4669–4674.
17 I. S. Veshchunov, W. Magrini, S. V. Mironov, A. G. Godin, J.-B. Trebbia, A. I. Buzdin, P. Tamarat and B. Lounis, *Nat. Commun.*, 2016, **7**, 12801.
18 V. Vlasko-Vlasov, A. Rydh, R. Divan, D. Rosenmann, A. Glatz and W.-K. Kwok, *J. Magn. Magn. Mater.*, 2022, **557**, 169476.
19 J. Parisi, R. P. Huebener and B. Mühlemeier, *Appl. Phys. Lett.*, 1982, **40**, 907–909.
20 Z. Bak, Multi-quanta Abrikosov vortices as the micro spin batteries, *arxiv*, 2024, preprint, **https://arxiv.org/abs/2412.05118**.
21 T. Golod, A. Iovan and V. M. Krasnov, *Nat. Commun.*, 2015, **6**, 8628.
22 J. E. Villegas, S. Savel'ev, F. Nori, E. M. Gonzalez, J. V. Anguita, R. García and J. L. Vicent, *Science*, 2003, **302**, 1188–1191.
23 D. Cole, S. Bending, S. Savel'ev, A. Grigorenko, T. Tamegai and F. Nori, *Nat. Mater.*, 2006, **5**, 305–311.
24 C. C. de Souza Silva, A. V. Silhanek, J. Van de Vondel, W. Gillijns, V. Metlushko, B. Ilic and V. V. Moshchalkov, *Phys. Rev. Lett.*, 2007, **98**, 117005.
25 O. V. Dobrovolskiy, *Phys. C*, 2017, **533**, 80–90.
26 A. I. Braginski, *J. Supercond. Novel Magn.*, 2019, **32**, 23–44.
27 C. Song, M. P. DeFeo, K. Yu and B. L. T. Plourde, *Appl. Phys. Lett.*, 2009, **95**, 232501.
28 S. Eley, A. Glatz and R. Willa, *J. Appl. Phys.*, 2021, **130**, 050901.
29 D. A. Ivanov, *Phys. Rev. Lett.*, 2001, **86**, 268–271.
30 C.-K. Chiu, T. Machida, Y. Huang, T. Hanaguri and F.-C. Zhang, *Sci. Adv.*, 2020, **6**, eaay0443.
31 A. I. Buzdin, *Rev. Mod. Phys.*, 2005, **77**, 935–976.
32 I. F. Lyuksyutov and V. L. Pokrovsky, *Adv. Phys.*, 2005, **54**, 67–136.
33 A. Palau, S. Valencia, N. Del-Valle, C. Navau, M. Cialone, A. Arora, F. Kronast, D. A. Tennant, X. Obradors, A. Sanchez and T. Puig, *Adv. Sci.*, 2016, **3**, 1600207.
34 N. Del-Valle, S. Agramunt-Puig, A. Sanchez and C. Navau, *Appl. Phys. Lett.*, 2015, **107**, 133103.
35 M. V. Milošević and F. M. Peeters, *Phys. Rev. Lett.*, 2004, **93**, 267006.
36 W. Gillijns, M. V. Milošević, A. V. Silhanek, V. V. Moshchalkov and F. M. Peeters, *Phys. Rev. B: Condens. Matter Mater. Phys.*, 2007, **76**, 184516.
37 R. B. G. Kramer, A. V. Silhanek, W. Gillijns and V. V. Moshchalkov, *Phys. Rev. X*, 2011, **1**, 021004.
38 F. Bobba, C. Di Giorgio, A. Scarfato, M. Longobardi, M. Iavarone, S. A. Moore, G. Karapetrov, V. Novosad, V. Yefremenko and A. M. Cucolo, *Phys. Rev. B: Condens. Matter Mater. Phys.*, 2014, **89**, 214502.
39 H. M. Jafri, H. Huang, C. Yang, J. Wang, A. A. Amirov, L.-Q. Chen and C.-W. Nan, *J. Phys. D: Appl. Phys.*, 2020, **53**, 375001.
40 S. M. Dahir, A. F. Volkov and I. M. Eremin, *Phys. Rev. B*, 2020, **102**, 014503.
41 B. Niedzielski and J. Berakdar, *Phys. Status Solidi B*, 2020, **257**, 1900709.
42 A. Gutfreund, H. Matsuki, V. Plastovets, A. Noah, L. Gorzawski, N. Fridman, G. Yang, A. Buzdin, O. Millo, J. W. A. Robinson and Y. Anahory, *Nat. Commun.*, 2023, **14**, 1630.
43 A. P. Petrović, M. Raju, X. Y. Tee, A. Louat, I. Maggio-Aprile, R. M. Menezes, M. J. Wyszyński, N. K. Duong, M. Reznikov, C. Renner, M. V. Milošević and C. Panagopoulos, *Phys. Rev. Lett.*, 2021, **126**, 117205.
44 B. Oripov and S. M. Anlage, *Phys. Rev. E*, 2020, **101**, 033306.
45 S. A. Díaz, J. Nothhelfer, K. M. D. Hals and K. Everschor-Sitte, *Phys. Rev. B*, 2024, **109**, L201110.
46 O. V. Dobrovolskiy, R. Sachser, T. Brächer, T. Böttcher, V. V. Kruglyak, R. V. Vovk, V. A. Shklovskij, M. Huth, B. Hillebrands and A. V. Chumak, *Nat. Phys.*, 2019, **15**, 477–482.
47 M. Borst, P. H. Vree, A. Lowther, A. Teepe, S. Kurdi, I. Bertelli, B. G. Simon, Y. M. Blanter and T. van der Sar, *Science*, 2023, **382**, 430–434.

48 J. Kharlan, K. Sobucki, K. Szulc, S. Memarzadeh and J. W. Kłos, *Phys. Rev. Appl.*, 2024, **21**, 064007.
49 G. Yang, C. Ciccarelli and J. W. A. Robinson, *APL Mater.*, 2021, **9**, 050703.
50 A. S. Melnikov, S. V. Mironov, A. V. Samokhvalov and A. I. Buzdin, *Phys.-Usp.*, 2022, **65**, 1248–1289.
51 K.-R. Jeon, X. Montiel, S. Komori, C. Ciccarelli, J. Haigh, H. Kurebayashi, L. F. Cohen, A. K. Chan, K. D. Stenning, C.-M. Lee, M. Eschrig, M. G. Blamire and J. W. A. Robinson, *Phys. Rev. X*, 2020, **10**, 031020.
52 I. A. Golovchanskiy, N. N. Abramov, V. S. Stolyarov, P. S. Dzhumaev, O. V. Emelyanova, A. A. Golubov, V. V. Ryazanov and A. V. Ustinov, *Adv. Sci.*, 2019, **6**, 1900435.
53 B. Niedzielski, C. Jia and J. Berakdar, *Phys. Rev. Appl.*, 2023, **19**, 024073.
54 R. Steiner and P. Ziemann, *Phys. Rev. B: Condens. Matter Mater. Phys.*, 2006, **74**, 094504.
55 E. Zhakina, L. Turnbull, W. Xu, M. König, P. Simon, W. Carrillo-Cabrera, A. Fernandez-Pacheco, U. Vool, D. Suess, C. Abert, V. M. Fomin and C. Donnelly, Vortex motion in reconfigurable three-dimensional superconducting nano-architectures, *arxiv*, 2024, preprint, **https://arxiv.org/abs/2404.12151**.
56 V. A. Schweigert, F. M. Peeters and P. S. Deo, *Phys. Rev. Lett.*, 1998, **81**, 2783–2786.
57 T. S. Alstrøm, M. P. Sørensen, N. F. Pedersen and S. Madsen, *Acta Appl. Math.*, 2011, **115**, 63–74.
58 C. A. Aguirre, M. R. Joya and J. Barba-Ortega, *J. Low Temp. Phys.*, 2017, **186**, 250–258.
59 J. D. González, J. Barón-Jaimez and J. Barba-Ortega, *J. Low Temp. Phys.*, 2015, **179**, 264–275.
60 V. L. Ginzburg and L. D. Landau, *On the Theory of Superconductivity*, Springer, Berlin, Heidelberg, 2009, pp. 113–137.
61 A. Gulian, *Shortcut to Superconductivity*, Springer, Cham, Switzerland, 1st edn, 2020, pp. XVII, 276.
62 I. Mowgood, G. Melkonyan, R. Dulal, S. Teknowijoyo, S. Chahid and A. Gulian, *Supercond. Sci. Technol.*, 2022, **35**, 045006.
63 L. P. Gor'kov and G. M. Eliasberg, *Generalization of the Ginzburg–Landau equations for non-stationary problems in the case of alloys with paramagnetic impurities*, World Scientific, 1996, pp. 16–22.
64 A. Schmid, *Phys. Kondens. Mater.*, 1966, **5**, 302–317.
65 J. E. Lee, J. Choi, T. S. Jung, J. H. Kim, Y. J. Choi, K. I. Sim, Y. Jo and J. H. Kim, *Nat. Commun.*, 2023, **14**, 2737.
66 L. Bishop-Van Horn, *Comput. Phys. Commun.*, 2023, **291**, 108799.
67 W. B. Zimmerman, *Multiphysics modeling with finite element methods*, World Scientific Publishing Company, 2006, vol. 18.
68 COMSOL AB, Stockholm, Sweden, COMSOL Multiphysics Modeling Guide, Version 3.5a, 2009.
69 C. Berthod, *Phys. Rev. B: Condens. Matter Mater. Phys.*, 2005, **71**, 134513.
70 E. D. V. Niño, A. Díaz-Lantada and J. Barba-Ortega, *J. Low Temp. Phys.*, 2019, **195**, 202–210.
71 Z. Huda, *Creep Behavior of Materials*, Springer International Publishing, Cham, 2022, pp. 253–265.
72 S. Lemerle, J. Ferré, C. Chappert, V. Mathet, T. Giamarchi and P. Le Doussal, *Phys. Rev. Lett.*, 1998, **80**, 849–852.
73 T. Tybell, P. Paruch, T. Giamarchi and J.-M. Triscone, *Phys. Rev. Lett.*, 2002, **89**, 097601.
74 G. Blatter, M. V. Feigel'man, V. B. Geshkenbein, A. I. Larkin and V. M. Vinokur, *Rev. Mod. Phys.*, 1994, **66**, 1125–1388.
75 D. A. Beloglazov and D. A. Kuptsov, *J. Phys. I Fr.*, 1992, **2**, 423–431.
76 M. Buchacek, R. Willa, V. B. Geshkenbein and G. Blatter, *Phys. Rev. B*, 2019, **100**, 014501.
77 D. R. Nelson and V. M. Vinokur, *Phys. Rev. B: Condens. Matter Mater. Phys.*, 1993, **48**, 13060–13097.
78 M. Baert, V. V. Metlushko, R. Jonckheere, V. V. Moshchalkov and Y. Bruynseraede, *Phys. Rev. Lett.*, 1995, **74**, 3269–3272.
79 V. G. Kogan, L. N. Bulaevskii, P. Miranović and L. Dobrosavljević-Grujić, *Phys. Rev. B: Condens. Matter Mater. Phys.*, 1995, **51**, 15344–15350.
80 A. Gurevich and G. Ciovati, *Phys. Rev. B: Condens. Matter Mater. Phys.*, 2013, **87**, 054502.
81 M. Timmermans, T. Samuely, B. Raes, J. Van de Vondel and V. V. Moshchalkov, *ACS Nano*, 2014, **8**, 2782–2787.
82 J.-Y. Ge, V. N. Gladilin, J. Tempere, C. Xue, J. T. Devreese, J. Van de Vondel, Y. Zhou and V. V. Moshchalkov, *Nat. Commun.*, 2016, **7**, 13880.
83 J. C. Keay, P. R. Larson, K. L. Hobbs, M. B. Johnson, J. R. Kirtley, O. M. Auslaender and K. A. Moler, *Phys. Rev. B: Condens. Matter Mater. Phys.*, 2009, **80**, 165421.
84 A. Correa, F. Mompeán, I. Guillamón, E. Herrera, M. García-Hernández, T. Yamamoto, T. Kashiwagi, K. Kadowaki, A. I. Buzdin, H. Suderow and C. Munuera, *Commun. Phys.*, 2019, **2**, 1–7.
85 L. Embon, Y. Anahory, Ž. L. Jelić, E. O. Lachman, Y. Myasoedov, M. E. Huber, G. P. Mikitik, A. V. Silhanek, M. V. Milošević, A. Gurevich and E. Zeldov, *Nat. Commun.*, 2017, **8**, 85.
86 C. Donnelly, M. Guizar-Sicairos, V. Scagnoli, S. Gliga, M. Holler, J. Raabe and L. J. Heyderman, *Nature*, 2017, **547**, 328–331.
87 O. Mathon, P. Van Der Linden, T. Neisius, M. Sikora, J. M. Michalik, C. Ponchut, J. M. De Teresa and S. Pascarelli, *J. Synchrotron Radiat.*, 2007, **14**, 409–415.

